Article

Direct Dioxygen Radical Coupling Driven by Octahedral Ruthenium−Oxygen−Cobalt Collaborative Coordination for Acidic Oxygen Evolution Reaction

Weijie Zhu, Fen Yao,* Kangjuan Cheng, Mengting Zhao, Cheng-Jie Yang, Chung-Li Dong,*
Qiming Hong, Qiu Jiang,* Zhoucheng Wang, and Hanfeng Liang*

Cite This: https://doi.org/10.1021/jacs.3c05556

Read Online

ACCESS | 📊 Metrics & More | 📖 Article Recommendations | 🆂🅸 Supporting Information

ABSTRACT: The acidic oxygen evolution reaction (OER) has long been the bottleneck of proton exchange membrane water electrolyzers given its harsh oxidative and corrosive environments. Herein, we suggest an effective strategy to greatly enhance both the acidic OER activity and stability of Co_3O_4 spinel by atomic Ru selective substitution on the octahedral Co sites. The resulting highly symmetrical octahedral Ru−O−Co collaborative coordination with strong electron coupling effect enables the direct dioxygen radical coupling OER pathway. Indeed, both experiments and theoretical calculations reveal a thermodynamically breakthrough heterogeneous diatomic oxygen mechanism. Additionally, the active Ru−O−Co units are well-maintained upon the acidic OER thanks to the electron transfer from surrounding electron-enriched tetrahedral Co atoms *via* bridging oxygen bonds that suppresses the overoxidation and thus dissolution of active Ru and Co species. Consequently, the prepared catalyst, even with a low Ru mass loading of *ca.* 42.8 $\mu g\ cm^{-2}$, exhibits an attractive acidic OER performance with a low overpotential of 200 mV and a low potential decay rate of 0.45 mV h^{-1} at 10 mA cm^{-2}. Our work suggests an effective strategy to significantly enhance both the acidic OER activity and stability of low-cost electrocatalysts.
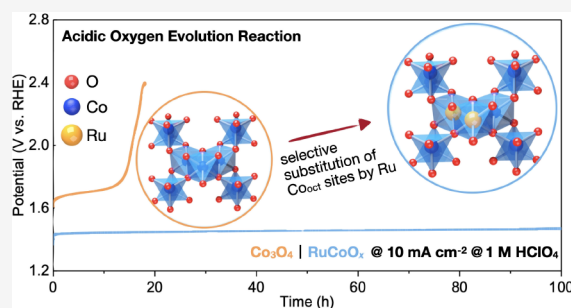
INTRODUCTION

Water electrolysis is considered as an environmental-friendly technology for green hydrogen production. Compared with the commercially available alkaline water electrolyzer, the acidic proton exchange membrane water electrolyzer (PEMWE) possesses several advantages, including lower ohmic resistance, higher current densities, better compatibility with sustainable energy resources, *etc.*[1−3] The development of the PEMWE, however, has long been limited by the anodic oxygen evolution reaction (OER), due to the lack of effective and stable electrocatalysts as most known electrocatalysts would suffer from corrosion and dissolution under the strongly acidic and oxidative conditions. Even for the state-of-the-art noble metal Ru-based materials, the stability is still unsatisfactory because of the formation of soluble species (*e.g.*, RuO_4) during the acidic OER.[4−6] Previous studies also demonstrated that the OER over RuO_2 is dominated by lattice oxygen mechanism (LOM), which involves the continuous insertion and extraction of lattice oxygens and thus would destroy the structural stability.[7−10]

In addition to the severe performance decay, the high price and scarcity of Ru (*ca.* $17,420 kg^{-1}) are also a big concern. The noble metal content in Ru-based catalysts (*e.g.*, transition metal-doped RuO_2,[11−13] RuB_2,[14] Ru/RuS_2[15]) is usually more than 80 wt %, and the Ru mass loading is typically higher than

0.2 mg cm^{-2} in three-electrode tests or 2 mg cm^{-2} in PEMWE in order to achieve decent performance. Therefore, enormous efforts have been devoted to lowering the Ru usage by improving the utilization efficiency (*e.g.*, through loading highly dispersed clusters or even single atoms on acid-resistant supports) or further, by directly using non-noble catalysts.[16−20]
In this regard, Co_3O_4 has been considered as a promising alternative. Previous studies have revealed that Co_3O_4 delivers an acceptable OER stability in acidic electrolytes, yet its activity requires further enhancement.[21−24] The Co_3O_4 shares a spinel AB_2O_4 structure, where Co^{II} ions occupy the tetrahedral A sites and Co^{III} ions occupy the octahedral B sites, respectively. The latter has been demonstrated to be significantly more active than the former for OER.[25] This is confirmed by the fact that the $ZnCo_2O_4$ (where Zn atoms occupy the tetrahedral sites only) shows comparable OER activity as that of Co_3O_4,[26] while the $CoAl_2O_4$ (where Al atoms
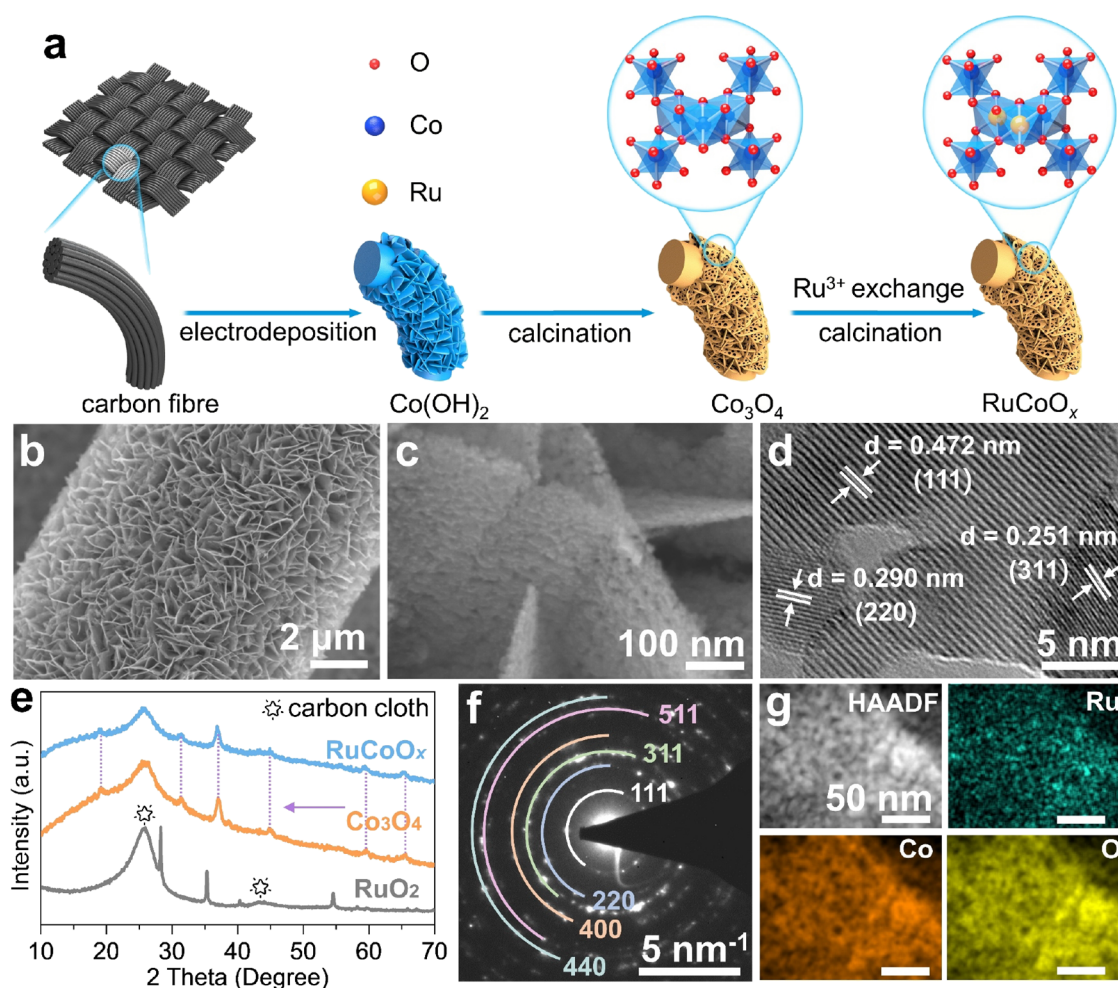
Figure 1. Synthesis of the RuCoO$_x$. (a) Schematic illustration of the synthetic process. (b, c) SEM and (d) HRTEM images of the RuCoO$_x$. (e) XRD patterns of the RuO$_2$, Co$_3$O$_4$ and RuCoO$_x$. (f) SAED patterns of the RuCoO$_x$. (g) HAADF-STEM image and the corresponding elemental maps of the RuCoO$_x$.

occupy the octahedral sites) possesses weaker activity than Co$_3$O$_4$.[27] The engineering of octahedral Co (*i.e.*, Co$_{oct}$) sites, for instance, by atomic substitution, therefore provides an effective way to regulate the coordination environment of Co$_3$O$_4$ and further boost the OER performance. In addition, previous studied have demonstrated a diatomic oxygen mechanism (DOM) over Co$_3$O$_4$ for OER.[28−32] The DOM proceeds with direct dioxygen radicals coupling to release O$_2$, which can effectively circumvent the formation of the *OOH intermediate and thus break the *OH and *OOH scaling relationship limitation of the traditional adsorbate evolution mechanism (AEM).[33,34] In this regard, the precise substitution of octahedral Co with other atoms might also enable the DOM pathway and significantly enhance the acidic OER performance, though it has not been realized yet.

In this work, we developed a modified Co$_3$O$_4$ spinel electrocatalyst with atomic Ru substitution on the Co$_{oct}$ sites (named as RuCoO$_x$ thereafter). The construction of highly symmetrical Ru$_{oct}$−O−Co$_{oct}$ collaborative coordination with a strong electron coupling effect significantly shortens the spatial distance between Ru$_{cot}$ and Co$_{cot}$, which makes the direct dioxygen radical coupling become favorable. Indeed, we confirmed both experimentally and theoretically that a thermodynamically breakthrough heterogeneous DOM driven by the Ru$_{oct}$−O−Co$_{oct}$ collaborative coordination is preferred,

rather than the theoretically limited AEM and the structurally unstable LOM that are more commonly observed. More importantly, the strong interaction of the Ru$_{oct}$−O−Co$_{oct}$ collaborative coordination is also well-maintained upon the acidic OER due to the electron capture from surrounding electron-enriched tetrahedral Co (*i.e.*, Co$_{tet}$) atoms *via* bridging oxygen bonds. As a result, the RuCoO$_x$ exhibits significantly enhanced OER activity and stability in acid even with a low Ru loading of *ca.* 42.8 μg cm^{-2}. Specifically, the RuCoO$_x$ delivers a small overpotential of 200 mV at 10 mA cm^{-2} and can steadily operate for at least 100 h with an only 45 mV potential decay. Further, the assembled PEMWE based on the commercial 20 wt % Pt/C and RuCoO$_x$ combination also shows outstanding stability even at a higher current density of 100 mA cm^{-2}.

■ RESULTS AND DISCUSSION

Catalyst Synthesis and Structural Characterization. The RuCoO$_x$ catalyst with Ru$_{oct}$ substitution was synthesized on carbon cloth substrate by a cation exchange strategy. In a typical synthesis, the Co(OH)$_2$ nanosheets were first electrodeposited onto carbon cloth followed by calcination to produce the porous Co$_3$O$_4$ nanosheets precursor, which was then immersed in a RuCl$_3$ aqueous solution to initiate the cation exchange. The resulting product was then annealed into the anhydrous RuCoO$_x$ nanosheet catalyst (Figure 1a, see the
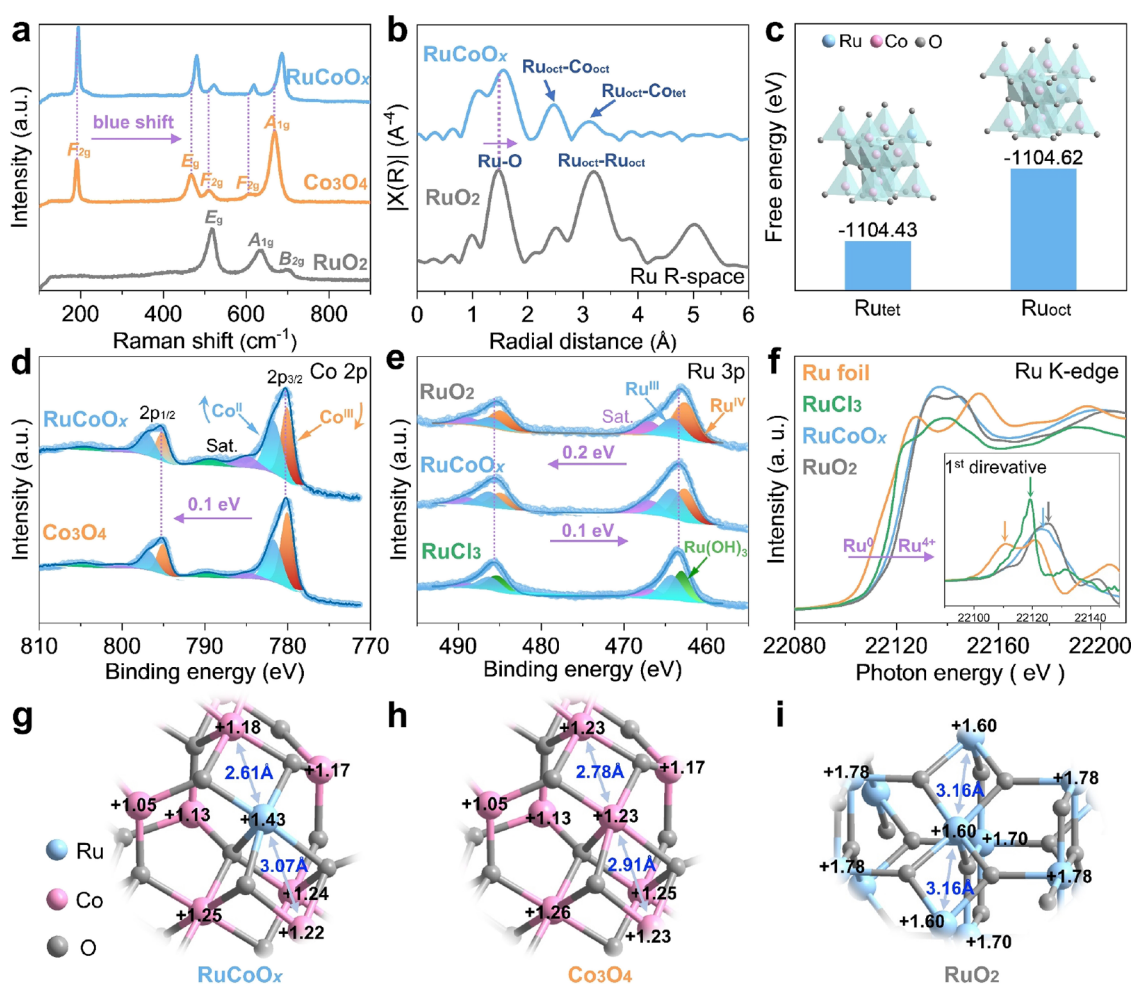
Figure 2. Identification of the $Ru_{oct}-O-Co_{oct}$ coordination environment in the $RuCoO_x$. (a) Raman spectra of the RuO_2, Co_3O_4 and $RuCoO_x$. (b) Ru FT-EXAFS spectra of the RuO_2 and $RuCoO_x$. (c) Energy diagram of a substituted Ru atom in the Co_3O_4. (d) Co 2p XPS spectra of the Co_3O_4 and $RuCoO_x$. (e) Ru 3p XPS spectra of the RuO_2, $RuCoO_x$, and $RuCl_3$ control. (f) Ru K-edge XANES spectra of the Ru foil, $RuCl_3$ control, $RuCoO_x$ and RuO_2; inset is the Ru K-edge 1st derivative spectra. Bader charge distribution diagrams of (g) $RuCoO_x$, (h) Co_3O_4, and (i) RuO_2.

principle of the cation exchange strategy in the Supporting Information). We systematically investigated the impacts of synthetic conditions and found that a cation exchange time of 9 h and a second calcination temperature of 250 °C would result in the optimal OER activity and operation stability (Figure S1). The conditions were then used for the rest of the study.

We first examined the structural difference between the Co_3O_4 and $RuCoO_x$. The SEM images show that both the porous Co_3O_4 and $RuCoO_x$ nanosheet array uniformly covers the surface of carbon fibers (Figure 1b,c and Figure S2a−c), forming an interconnected 3D network with close surface areas (12.36 and 13.36 m^2 g^{-1}, respectively, Figure S3a). A careful observation further reveals that both the Co_3O_4 and $RuCoO_x$ nanosheets are composed of abundant micropores with the same pore diameter distribution from 5 to 60 nm (Figures S2d, S3b, and S4). Although the $RuCoO_x$ largely inherits the overall morphology from the Co_3O_4 precursor, the lattice distance is sensitively expanded (*e.g.*, $d_{(311)}$ from 0.244 to 0.251 nm, and $d_{(220)}$ from 0.285 to 0.290 nm) as revealed by the high-resolution transmission electron microscopy (HRTEM) image (see comparison in Figure 1d and Figure S2e). This can be also confirmed by the X-ray diffraction (XRD) patterns (Figure 1e and Figure S5). Besides the two broad diffraction peaks

originated from the carbon cloth substrate (Figure S6), all the other diffraction peaks can be assigned to spinel Co_3O_4 (JCPDS card no. 74-1656). Notably, the overall diffraction peaks of the $RuCoO_x$ slightly shift to lower angles in comparison to those of the Co_3O_4, implying that the lattices of the Co_3O_4 are expanded because of the incorporation of Ru atoms with a larger radius. Moreover, no other Ru species are observed even after the thermal calcination of the $RuCoO_x$ at 800 °C in an Ar atmosphere (Figure S5), which not only rules out the existence of amorphous Ru species but also demonstrates the high structural stability of Ru atoms in the Co_3O_4 matrix. Indeed, the selected area electron diffraction (SAED) pattern of the $RuCoO_x$ also confirms that all the visible polycrystalline rings belong to Co_3O_4 (Figure 1f). Additionally, the high-angle annular dark-field scanning TEM (HAADF-STEM) image and its corresponding elemental maps reveal that the elemental distribution of the substituted Ru is highly consistent with that of Co and O signals (Figure 1g). These results suggest that the Ru atoms were doped into the Co_3O_4 lattice, instead of aggregating on the surface of the Co_3O_4 nanosheets as Ru or RuO_2 clusters.

The mass loadings of Ru and Co on carbon cloth were *ca.* 0.0428 and 2.3495 mg cm^{-2}, respectively, corresponding to a bulk Ru ratio of *ca.* 1.55 at. % (determined by inductively

coupled plasma mass spectrometry or ICP-MS, see details in the Supporting Information). Meanwhile, the surface Ru ratio, determined by X-ray photoelectron spectroscopy (XPS) analysis, was up to *ca.* 25 at. % (Figure S7). These results suggest that cation exchange reaction would lead to a concentration gradient of Ru from high to low along the surface to bulk, which improves the Ru utilization efficiency for the surface electrocatalysis reaction. The commercial RuO_2 on carbon cloth with a mass loading of 1 mg cm^{-2} was also prepared for comparison (see detailed characterizations in Figure S8).

Identification of Selective Ru Sites in the RuCoO$_x$. In order to reveal the selective substitution of Co sites (octahedral or tetrahedral) in the Co_3O_4 by Ru atoms, we then conducted the Raman test, which is a sensitive technology to reveal the changes in the coordination environment. The Co_3O_4 spinel presents five Raman-active modes (*i.e.*, A_{1g}, E_g, and three F_{2g} modes, Figure 2a). The characteristic Raman peaks of the RuCoO$_x$ are almost identical to those of Co_3O_4 but shift to the higher frequency region. Notably, the shift of A_{1g} (685 cm^{-1}) is more significant than that of F_{2g} band (195 cm^{-1}). Since the former is related to the stretching of Co^{III}−O in the octahedral (CoO_6) units while the latter raises from Co^{II}−O in the tetrahedral (CoO_4) groups,[35,36] thus we can reasonably infer that the Ru atoms preferentially occupy the position of Co_{oct} instead of Co_{tet} sites. Indeed, the decrease in peak intensity of A_{1g}/F_{2g} bands of the RuCoO$_x$ compared to that of the Co_3O_4 also suggests the decrease in the ratio of Co_{oct}/Co_{tet} due to the Ru_{oct} substitution.

We also employed the Fourier transformed (FT) k^3-weighted extended X-ray absorption fine structure (FT-EXAFS) analysis to identify the bonding environment. The Ru FT-EXAFS spectra indicate that a characteristic peak at 2.49 Å observed for the RuCoO$_x$ in the second shell (slightly larger than the Co_{oct}−Co_{oct} bond, 2.45 Å, without phase correction, Figure S9b) can be assigned to Ru_{oct}−Co_{oct} coordination, suggesting that Ru atoms successfully substitute partial Co_{oct} sites in the Co_3O_4. It is noted that the weakened and broadened FT peak at 3.13 Å in the higher shell likely belongs to the Ru_{oct}−Co_{tet} coordination, which is obviously different from the intense FT peak at 3.19 Å that assigned to the Ru_{oct}−Ru_{oct} coordination in the RuO_2. This can also exclude the existence of the pure RuO_2 phase in the RuCoO$_x$, well in line with the SAED and XRD results. Apart from the experimental spectroscopy characterizations, density functional theory (DFT) calculation also reveals that the required free energy of substituting one Ru atom into the Co_{oct} site is 0.19 eV lower than that into the Co_{tet} site (Figure 2c), further confirming the selective occupancy of Ru atoms in the octahedral Co sites of Co_3O_4.

Revelation of Strong Electron Coupling Effect in the RuCoO$_x$. The Ru_{oct} substitution in the Co_3O_4 is expected to modulate the surface electronic distribution and bonding environment. The surface-sensitive Co 2p XPS spectrum of the RuCoO$_x$ shows a upshift of *ca.* 0.1 eV compared to that of the Co_3O_4 (Figure 2d), suggesting the decrease in the Co_{oct}/Co_{tet} ratio (Table S1).[37,38] This is not only ascribed to the occupied octahedral sites by substituted Ru atoms as revealed before but also attributed to the partial electron transfer from Ru_{oct} to Co_{oct} atoms *via* bridging oxygen atoms in the RuCoO$_x$. The later can be further verified by the complementary Ru 3p XPS spectra (Figure 2e), wherein the overall binding energy of the RuCoO$_x$ is 0.2 eV higher than the RuO_2 but 0.1 eV lower than

that of the $RuCl_3$ control, and a more obvious trend was observed for the Ru 3d XPS spectra (Figure S10), meaning that the Ru oxidation state in the RuCoO$_x$ is between +3 and +4 (Table S1),[39,40] higher than the original Co_{oct} site (+3) in the Co_3O_4. It is noted that the existence of $Ru(OH)_3$ is inevitable due to the slight hydrolysis of the $RuCl_3$ in air.[39] The Ru oxidation state in the RuCoO$_x$ can be further identified by the Ru K-edge XANES and 1st derivative spectra (Figure 2f), wherein the absorption edge of the RuCoO$_x$ is higher than that of the $RuCl_3$ but lower than that of the RuO_2. Meanwhile, the energy of the maximum of 1st derivative of the RuCoO$_x$ displays the same trend (see detailed explanation in the Supporting Information). The lower Ru oxidation state in the RuCoO$_x$ than that in the RuO_2 would thus result in the longer bond length of Ru−O bonds (1.56 *vs* 1.47 Å, Figure 2b), which could be attributed to the increased extranuclear electron numbers of Ru centers in the RuCoO$_x$. The increased electron cloud density around active Ru sites has been demonstrated to be favorable to facilitating the acidic OER progress.[12,13,41] It is noted that the Co K-edge XANES spectra indicate that the Co oxidation state in the RuCoO$_x$ is almost identical to that in the Co_3O_4 (Figure S9a), and the corresponding distances of Co−O, Co_{oct}−Co_{oct}, and $Co_{oct/tet}$−Co_{tet} bonds in *R* space of FT-EXAFS spectra are also almost identical (Figure S9b). This is not surprising because the X-ray absorption spectroscopy is bulk sensitive, while the ion exchange most likely occurs on the surface of the Co_3O_4 given the trace amount of Ru (1.55 at. %) and thus would not significantly affect the bulk properties.

Considering that the XPS and XANES only identify the overall change of electronic structure of the Co_3O_4 after Ru_{oct} substitution, we further conducted the Bader charge analysis to explore the partial change of elemental charge distribution on the catalyst (near-)surface in detail. The substituted Ru_{oct} atom can significantly modulate the positive charge of one of the oxygen-bridging Co_{oct} atoms from +1.23|e| to +1.18|e| and slightly change the charge distribution of the other neighboring Co_{oct} sites, yet barely affect the surrounding Co_{tet} sites (see comparison between the RuCoO$_x$ and Co_3O_4 in Figure 2g,h). In addition, the Bader charge of the substituted Ru_{cot} atom (+1.43|e|) in the RuCoO$_x$ is obviously higher than that of the original Co_{oct} atom (+1.23|e|) in the Co_3O_4 but still lower than that of Ru atoms in the RuO_2 (*e.g.*, +1.78, +1.70, and + 1.60|e|, Figure 2i), which also strongly supports the Ru 3p XPS and Ru K-edge XANES results. Both results reveal that Ru_{oct} substitution in the Co_3O_4 would induce electron transfer from the Ru_{oct} atom to an adjacent Co_{oct} atom *via* bridging oxygen bonds, well in line with the XPS analysis. The resulted partial charge imbalance in the RuCoO$_x$ remarkably enhances the hybrid behavior of Ru_{oct}−O and Co_{oct}−O coordination, resulting in the strong electron coupling effect of the Ru_{oct}−O−Co_{oct} unit with the shortened atomic distance between Ru_{oct} and Co_{cot} (2.61 Å) in comparison to the corresponding Co_{oct}−Co_{oct} atomic distance (2.78 Å) in the Co_3O_4 (Figure 2g,h). The heterogeneous metal sites with shortened distance in the Ru_{oct}−O−Co_{oct} collaborative coordination (research focus thereafter) is more beneficial than neighboring Ru_{oct}−Co_{oct} sites (3.07 Å) to conducting direct dioxygen radical coupling for the heterogeneous DOM. It is noted that the various Bader charges of Co in the Co_3O_4 and RuCoO$_x$ can be attributed to the different coordination environments of (near-)surface and bulk atoms (Figure S11).

Apart from the local Bader charge analysis, we also calculated the partial band centers and adsorption ability of
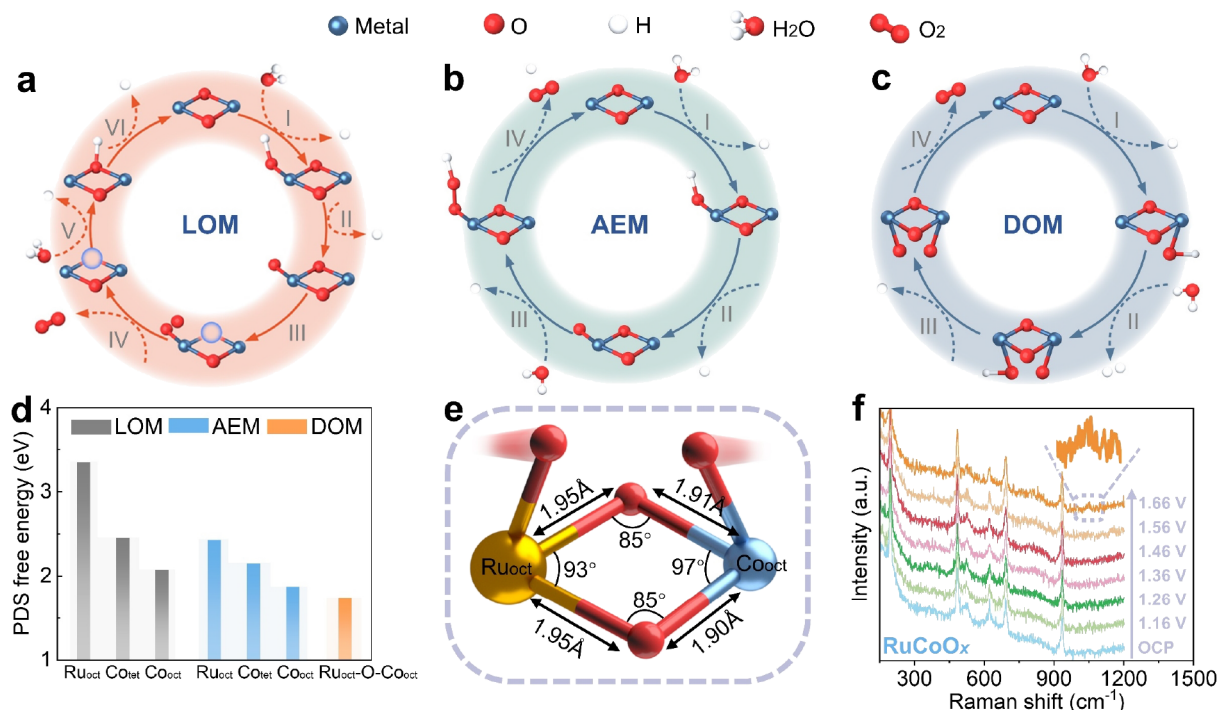
Figure 3. Identification of OER mechanism of the RuCoO$_x$. Schematic illustration of (a) LOM, (b) AEM, and (c) DOM reaction pathways. (d) Comparison of the PDS energy barrier of three reaction pathways. (e) Simulative structural model of a Ru$_{oct}$−O−Co$_{oct}$ unit with two adsorbed oxygen radicals. (f) *In situ* Raman spectra under applied potentials.

water molecules. The result indicates that the substituted Ru$_{oct}$ atom in the Co$_3$O$_4$ can adjust the 3d band center of adjacent Co$_{oct}$ sites (from −1.41 to −1.48 eV) more significantly than that of surrounding Co$_{tet}$ sites (from −1.27 to −1.23 eV, Figure S12a,b). Additionally, the Ru$_{oct}$ 4d band center in the RuCoO$_x$ also distinctly downshifts compared with those in the RuO$_2$ (−2.00 *vs* −1.37 or −1.46 eV, Figure S12a,c). Compared with Co sites in the Co$_3$O$_4$ and Ru sites in the RuO$_2$, the optimized band centers in the RuCoO$_x$ contribute to strengthening the water molecule adsorption ability of the Ru$_{oct}$−O−Co$_{oct}$ units in acid (Figure S13), which is favorable to accelerating the subsequent OER steps. Interestingly, we found that the O 2p band centers in the Ru$_{oct}$−O−Co$_{oct}$ units also display the obvious downward shift in comparison to those in the Co$_3$O$_4$ and RuO$_2$ (Figure S12), suggesting that lattice oxygens would not participate in the OER pathway, *i.e.*, the LOM pathway is not preferred. Whereas, for the RuO$_2$, its O 2p band centers are closest to the Fermi level (Figure S12c). Meanwhile, the formed strongest Ru 4d-O 2p orbital hybridization (the closest band center distance between Co 3d/Ru 4d and O 2p orbitals, Figure S12) would facilitate the lattice oxygen activation and subsequently trigger the LOM reaction pathway,[8,18,42] thereby causing inevitable structural deformation or even collapse and further the performance decay. Indeed, our DFT calculation reveals that the rutile RuO$_2$ (110) facet with the lowest thermodynamic surface energy prefers to follow the LOM rather than the AEM reaction pathway (Figure S14, Tables S2 and S3). The LOM on the RuO$_2$ was also experimentally confirmed by ^{18}O isotope-labeled differential electrochemical mass spectrometry (DEMS) in previous studies.[7−10] In addition to the formation of Ru$_{oct}$−O−Co$_{oct}$ collaborative coordination with a strong electron coupling effect and enhanced water adsorption ability, the substitution of Co$_{oct}$ sites by Ru atoms might also slightly

cause structural distortion and thus create defects. Both the O 1s XPS spectra and electron paramagnetic resonance (EPR) analysis reveal that the RuCoO$_x$ possesses more oxygen vacancies than the Co$_3$O$_4$ and RuO$_2$ (Figures S15 and S16, Table S1).

Identification of Acidic OER Mechanism of the RuCoO$_x$. Given the unique coordination environment and strong interaction of the Ru$_{oct}$−O−Co$_{oct}$ units in the RuCoO$_x$, we then conducted DFT calculation to explore the OER reaction pathway. According to the XRD result and previously reported articles, we used the spinel Co$_3$O$_4$ (311) facet with Ru$_{oct}$ substitution as the model (Figure S17).[22,43] We first evaluated the two well-accepted OER mechanisms (*i.e.*, AEM and LOM) for the RuCoO$_x$ (Figure 3a and b). The calculation result indicates that the potential determining step (PDS) of the RuCoO$_x$ following the AEM reaction pathway is the dehydrogenation step on the Co$_{oct}$ sites (1.88 eV, Figure S18a, Table S2), while the O−O coupling step by lattice oxygen activation follows the LOM reaction pathway at the same sites (2.07 eV, Figure S18b, Table S3). The maximum Gibbs free energy of the AEM is lower than that of the LOM reaction pathway (Figure 3d), meaning that the AEM pathway is preferred over the RuCoO$_x$. However, we consider that the Ru sites are much more active than Co$_{oct}$ sites in theory,[44,45] and in fact, the OER process over Ru$_{oct}$ sites in the RuCoO$_x$ is only significantly hindered by the transformation of *O to *OOH intermediates (2.43 eV), while the adsorption of *OH intermediate (0.25 eV) and the subsequent dehydrogenation (0.75 eV) proceed much easier (Figure S18a, Table S2). This indicates that the OER over the RuCoO$_x$ could possibly proceed with an unusual DOM reaction pathway driven by the heteroatomic Ru$_{oct}$−O−Co$_{oct}$ units. The DOM involves the adsorption of the *OH intermediate, the subsequent dehydrogenation, and the final dioxygen radical coupling
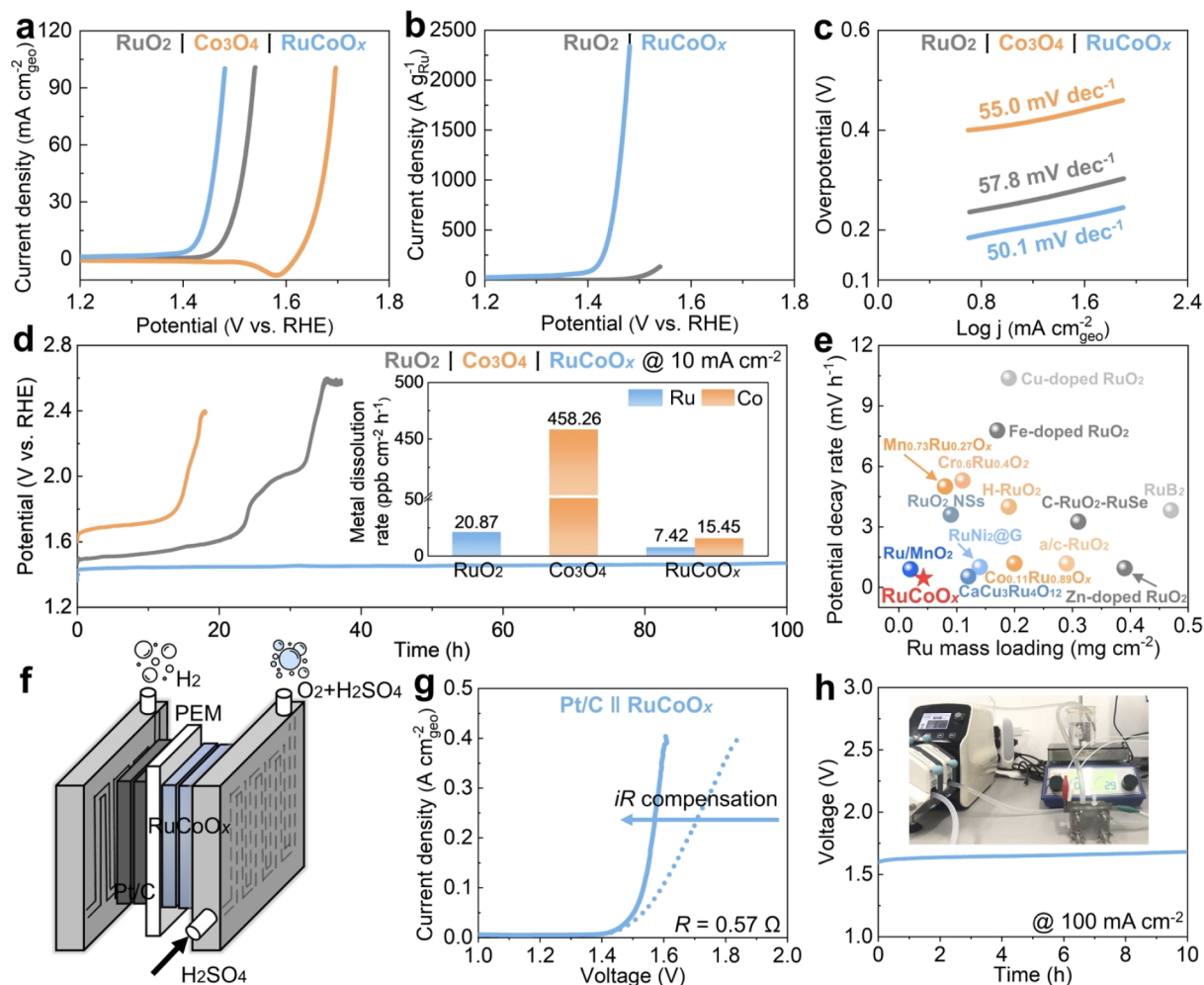
Figure 4. Acidic OER performance of the RuCoO$_x$. (a) Geometric LSV curves of the RuO$_2$, Co$_3$O$_4$ and RuCoO$_x$. (b) Ru mass normalized LSV curves of the RuO$_2$ and RuCoO$_x$. (c) Tafel plots of the RuO$_2$, Co$_3$O$_4$ and RuCoO$_x$. (d) Chronopotentiometry curves of the RuO$_2$, Co$_3$O$_4$, and RuCoO$_x$ at 10 mA cm^{-2} (inset shows the average metal dissolution rate). (e) Comprehensive evaluation of potential decay rates and Ru mass loading of the RuCoO$_x$ and other recently reported high-performance acidic OER electrocatalysts. (f) Schematic illustration of the PEMWE configuration using the RuCoO$_x$ and Pt/C couple. (g) Geometric LSV curves of the PEMWE. (h) Chronopotentiometry curves of the PEMWE at 100 mA cm^{-2} (inset shows the optical photograph of the device).

process (Figure 3c), which has been widely studied in theoretical and experimental aspects.[28−34] We then further calculated the bond lengths and the bond angles of the Ru$_{oct}$−O−Co$_{oct}$ units and found that they are highly symmetrical (Figure 3e) along with shortened atomic distances (Figure 2g). Both are beneficial to conducting the final O−O radical coupling with a low thermodynamic energy barrier.[34,46,47] Indeed, our simulation shows that the required free energy of the dioxygen radical coupling to form O$_2$ is as low as 1.17 eV (Figure S19a, Table S4), which further suggests that the OER over the RuCoO$_x$ might proceed with the DOM reaction pathway. In this case, the PDS would be the dehydrogenation of *OH intermediate on the Ru$_{oct}$ site (step III in Figure 3c), which requires a free energy of 1.74 eV (Figure 19a, Table S4), lower than that of the RuCoO$_x$ via the AEM or LOM reaction pathway (1.88 and 2.07 eV, respectively, Figure 3d) and that of the RuO$_2$ following the favorable LOM reaction pathway (2.16 eV, Figure S14). In addition, we also investigated the Ru$_{oct}$−O−Co$_{tet}$ coordination environment, and the bond lengths of Ru$_{oct}$−O and Co$_{tet}$−O are 2.00 and 1.87 Å, respectively (Figure S20). The unsymmetrical Ru$_{oct}$−O−Co$_{tet}$ units would lead to a much higher energy barrier for the dioxygen radical

coupling (2.11 eV, Figure S19b, Table S4), which thus becomes the PDS. We also evaluated dual Ru$_{oct}$ sites, dual Co$_{oct}$ sites, and the combination of Co$_{oct}$ and Co$_{tet}$ sites in the RuCoO$_x$ (Figure S19c−e, Table S4). The result demonstrates that the thermodynamic free energies of these dual sites at the PDSs are higher than that of the cooperative Co$_{oct}$ and Ru$_{oct}$ sites. Accordingly, the DFT calculation results reveal that the OER over the RuCoO$_x$ catalyst proceeds with the heterogeneous DOM reaction pathway thanks to the highly symmetrical and contractive Ru$_{oct}$−O−Co$_{oct}$ collaborative coordination, which has not been discovered so far.

The dioxygen radical coupling, which can be captured by *in situ* electrochemical techniques,[34,48−50] reliably distinguishes the DOM from the AEM and LOM. To experimentally confirm the O−O radical coupling, we then carried out the *in situ* Raman test in 0.1 M HClO$_4$. As shown in Figure 3f, when the applied potential is up to 1.66 V *vs* RHE (without *iR* correction) for the RuCoO$_x$, the Raman shift at around 1050 cm^{-1} assigned to dioxygen radical coupling appears,[50−52] which strongly supports the heterogeneous DOM reaction pathway of the RuCoO$_x$. We noted that the signal is relatively weak, but unfortunately failed to enhance the intensity either

by prolonging the test time or applying higher potentials, as the large amount of generated oxygen bubbles would interfere with the Raman incident light. It is also noted that the Raman signals assigned to Co−*OOH (~600 cm^{-1}) or Ru−*OOH (~720 cm^{-1}) are not detected, thereby excluding the possibility of the AEM over the RuCoO$_x$.[23,50,53] In brief, we confirmed both theoretically and experimentally that the RuCoO$_x$ catalyst prefers a thermodynamically breakthrough heterogeneous DOM driven by the Ru$_{oct}$−O−Co$_{oct}$ collaborative coordination.

Acidic OER Performance of the RuCoO$_x$. Given that the DOM can effectively circumvent the thermodynamic energy barrier step (*i.e.*, the formation of the *OOH intermediate) and thus break the *OH and *OOH scaling relationship limitation of the AEM, the RuCoO$_x$ catalyst is expected to exhibit higher activity than the state-of-the-art RuO$_2$ and Co$_3$O$_4$ catalysts. To further verify the inference, we then conducted the acidic OER measurements in a 1 M HClO$_4$ electrolyte that is much harsher than the commonly used 0.1 M HClO$_4$. The Hg/Hg$_2$SO$_4$ reference electrode was calibrated against reversible hydrogen electrode (RHE) using a cyclic voltammetry (CV) method (Figure S21).[54] Linear sweep voltammetry (LSV) curves display that the RuCoO$_x$ only requires a small overpotential of 200 mV to reach the benchmark current density of 10 mA cm^{-2}, much lower than that of the RuO$_2$ and Co$_3$O$_4$ (265 and 409 mV, respectively, Figure 4a). It is noted that the activity of the commercial RuO$_2$ is comparable to the reported value in the literature (Table S5). Although the RuCoO$_x$ exhibits a comparable geometric activity to other recently reported high-performance acidic OER electrocatalysts, its mass activity (*e.g.*, 2278 A g$_{Ru}^{-1}$ at 1.48 V *vs* RHE, Figure 4b) is significantly higher than the RuO$_2$ and most of the Ru or Ir-based catalysts (Figure 4b, Table S6). We also measured the electrochemically active surface area (ECSA) by evaluating the double layer capacitance (C$_{dl}$) (Figures S22−S24). The result shows that the calculated ECSA of the RuCoO$_x$ (5.70 cm^2) is larger than that of the RuO$_2$ and Co$_3$O$_4$ (1.58 and 5.42 cm^{-2}, respectively). It is noted that the RuCoO$_x$ still possesses the largest ECSA or BET normalized currents (Figures S25 and S26), suggesting the highest intrinsic activity among the three catalysts. This is further confirmed by the turnover frequency (TOF), which presents the transfer number of molecules per surface active site per unit time. For example, the RuCoO$_x$ achieves an 8.5-fold higher TOF (0.51 s^{-1}) than the RuO$_2$ (0.06 s^{-1}) at 1.48 V *vs* RHE, while the Co$_3$O$_4$ has no detectable OER currents at the same potential (Figures S27 and S28).

Besides the high activity, the RuCoO$_x$ also possesses the smallest geometric Tafel slope among three catalysts (Figure 4c), suggesting that the Ru$_{oct}$−O−Co$_{oct}$ coordination can accelerate the acidic OER kinetics. This is further confirmed by the electrochemical impedance spectroscopy (EIS) tests at a fixed potential of 1.43 V *vs* RHE, at which the RuCoO$_x$ exhibits the smallest film resistance (R$_f$) and charge transfer resistance (R$_{ct}$) compared to the RuO$_2$ and Co$_3$O$_4$ (Figure S29, Table S7). It is noted that we also fit the OER capacitance behavior (*i.e.*, Z$_{CPE2}$) of three electrodes and found that the trend is almost in accordance with the BET and roughness factor results (Table S8). All the evidence reveals that the thermodynamically breakthrough DOM contributes to the enhanced acidic OER activity of the RuCoO$_x$, superior to the Co$_3$O$_4$ and RuO$_2$.

We further examined the stability of the three catalysts at the benchmark current density of 10 mA cm^{-2} (Figure 4d). The operation stability of the OER electrocatalysts in acids has long been the bottleneck. Most transition metal oxides, including Co$_3$O$_4$,[24] WO$_3$,[55] and MnO$_2$,[56] cannot tolerate the harsh corrosive conditions. Even for the current state-of-the-art noble RuO$_2$ catalysts, the stability is still a big concern as they would easily form acidic soluble RuO$_4$ species with higher oxidation states under the highly oxidative and acidic environments.[4,5] Indeed, our result confirms that both the RuO$_2$ and Co$_3$O$_4$ suffer from fast performance decay with quickly elevated potentials within a few hours. Impressively, the RuCoO$_x$ can steadily operate for at least 100 h with an average degradation rate of only 0.45 mV h^{-1}. The acidic OER performance of the RuCoO$_x$, evaluated by both the low potential decay rate and noble metal mass loading, is superior to various recently reported high-performance Ru-based catalysts. (Figure 4e, and a more detailed comparison in Table S6). Notably, the average metal dissolution rate of the RuCoO$_x$ during the stability test is significantly slower than that of the RuO$_2$ and Co$_3$O$_4$, which is only ~1/3 and ~1/30 as that of the latter two, respectively (determined by ICP-MS, inset of Figure 4d). The stability number (S-number), defined as the amount of evolved O$_2$ when a metal atom dissolves in the electrolyte,[57] is another vital metric to evaluate the acidic OER stability and economic benefit. Since the cost of Ru (*ca.* $17,420 kg^{-1}) is nearly 400 times as that of Co (*ca.* $46 kg^{-1}), we therefore separately calculated the S-number of the RuCoO$_x$ based on dissolved Ru or Co metal. The calculated result indicates that the S-number of the RuCoO$_x$ per dissolved Ru atom (31774) is nearly 3 times as that of the RuO$_2$ (11297), while the S-number of the RuCoO$_x$ per dissolved Co atom (8895) is nearly 30 times as that of the Co$_3$O$_4$ (300) (Figure S30). In addition, the LSV curve of the RuCoO$_x$ after 1000 accelerated CV scans shows negligible changes (Figure S31), suggesting that it can withstand the frequent and intermittent power switching process.

We finally assembled a proton exchange membrane water electrolyzer (PEMWE) using two pieces of the RuCoO$_x$ as the anode and commercial 20 wt % Pt/C as the cathode, respectively (Figure 4f, see details in the Supporting Information). The PEMWE requires cell voltages of only 1.53, 1.56, and 1.60 V (after *iR* compensation) to drive the large current densities of 100, 200, and 400 mA cm^{-2}, respectively (Figure 4g). Moreover, the device can steadily operate at 100 mA cm^{-2} for continuous 10 h without obvious voltage fluctuation (Figure 4h), and the corresponding Faradaic efficiencies of H$_2$ and O$_2$ production reach *ca.* 97.29 and 90.94%, respectively (determined by water drainage method, Figure S32). The reduced Faradaic efficiency of the OER might be ascribed to the bubble accumulation in the rubber tubes and the possible slight oxidation of the carbon cloth substrate. It is worthy that the mass loading of precious Ru (*ca.* 85.6 μg cm^{-2}) used in the PEMWE is at least 20-fold less than that of other Ru-based PEMWE.[53,58,59]

Origin of the Acidic OER Stability of the RuCoO$_x$. The structural integrity of the RuCoO$_x$ after the 100 h of chronopotentiometry test was also investigated by the post physical characterizations. Electron microscope images and XRD patterns reveal no significant changes in the overall morphology and crystal structure (Figures S33 and S34). Moreover, the EPR spectra (Figure S35), together with the O 1s XPS spectra (Figure S36, Table S1), suggest an obvious
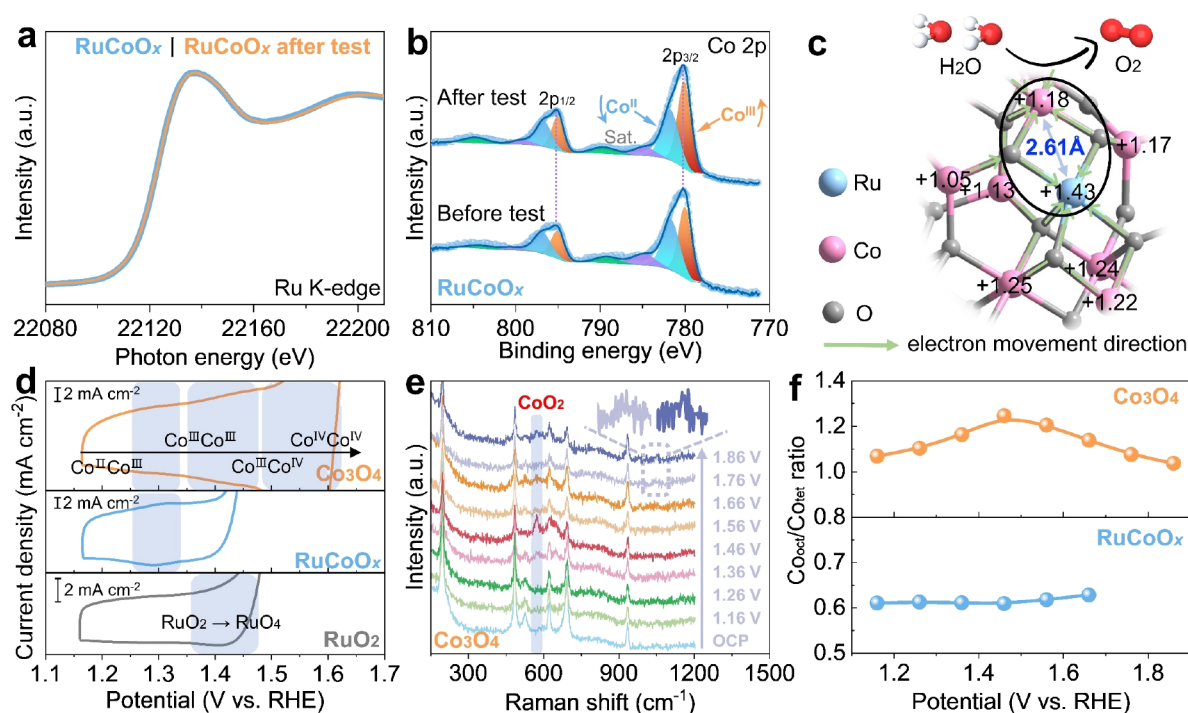
Figure 5. Acidic OER stability analysis. (a) Ru K-edge XANES and (b) Co 2p XPS spectra of the $RuCoO_x$ before and after the chronopotentiometry test. (c) Schematic illustration of electron migration in the $RuCoO_x$. (d) CV curves of the RuO_2, Co_3O_4, and $RuCoO_x$. (e) *In situ* Raman spectra of the Co_3O_4. (f) Co_{oct}/Co_{tet} ratio of the Co_3O_4 and $RuCoO_x$ under applied potentials.

decrease in oxygen vacancy concentration. This confirms that the oxygen vacancies are filled upon the OER, since the DOM requires a highly integral and symmetric structure. More importantly, we found that the Ru oxidation state is perfectly maintained after the long-term stability test, as revealed by the Ru K-edge XANES and XPS spectra (Figure 5a, Figure S37, and Table S1), though the $Ru_{oct}–Co_{oct}$ coordination is slightly weakened possibly due to the trace Ru dissolution, as revealed by Raman and FT-EXAFS spectra (Figures S38 and S39). This suggests the high structural integrity of the existing $Ru_{oct}–O–Co_{oct}$ units and thus the high acidic OER stability. In addition, the Ru_{oct}-Co_{tet} coordination is slightly stretched (Figure S39), which is likely due to the electrooxidation of Co_{tet} sites during the acidic OER. Indeed, the Co 2p XPS spectra indicate that the overall Co_{oct}/Co_{tet} ratio on the $RuCoO_x$ surface marginally increases (Figure 5b, Table S1). This is not surprising since the relatively electron-deficient $Ru_{oct}–O–Co_{oct}$ units with the strong electronic coupling effect can drag electrons from the adjacent electron-enriched Co (especially Co_{tet}) sites *via* bridging oxygen bonds during the OER electrocatalysis (Figure 5c),[60] which effectively prevents the overoxidation of active Ru_{oct} and Co_{oct} sites into acidic soluble RuO_4 and CoO_2 species, respectively, and thus maintains the acidic OER durability.

The above results confirm the structural integrity of active $Ru_{oct}–O–Co_{oct}$ collaborative coordination, which can also be reflected by comparing the CV curves of the three catalysts (Figure 5d and Figure S40). Three pairs of obvious redox couple at around 1.29, 1.45, and 1.56 V *vs* RHE for the Co_3O_4 are observed before OER currents, which can be assigned to the $Co^{II}Co^{III}/Co^{III}Co^{III}$, $Co^{III}Co^{III}/Co^{III}Co^{IV}$, and $Co^{III}Co^{IV}/Co^{IV}Co^{IV}$ redox reactions, respectively.[23,61] It is noted that though CoO_2 has been regarded as the active OER species in alkaline electrolytes for the majority of Co-based catalysts,[62–64]

it is highly dissolvable in acid, and thus the formation of CoO_2 would significantly degrade the OER stability (Figure 4d). For the RuO_2, we also observed a weak reduction peak around 1.41 V *vs* RHE assigned to RuO_4/RuO_2 redox reaction that is detrimental to the acidic OER durability.[65] Nonetheless, we only observed a pair of reversible and weak redox couple corresponding to the $Co^{II}Co^{III}/Co^{III}Co^{III}$ redox reaction for the $RuCoO_x$ prior to the OER onset potentials. This means that the $Ru_{oct}–O–Co_{oct}$ collaborative coordination with the strong electron coupling effect could promote the electrooxidation behavior of the adjacent Co_{tet} sites but not Co_{oct} and Ru_{oct} sites and thus capture electrons from oxidized Co_{tet} atoms so as to avoid the overoxidation of itself, well in line with the Co 2p XPS result. It should be noted that the failure of identifying the other redox couples from the CV of the $RuCoO_x$ does not necessarily mean that these redox reactions do not proceed. The oxidation currents might simply overlap with the OER currents and thus are difficult to differentiate. The inference that the overoxidation of active Co^{III} and Ru^{IV} sites in the $RuCoO_x$ is significantly suppressed, however, is also supported by the metal dissolution result before and the *in situ* Raman analysis later. As a result, the $RuCoO_x$ catalyst can maintain a decent acidic OER stability at 10 or even 100 mA cm^{-2}.

The outstanding stability of the $RuCoO_x$ can also be confirmed by the *in situ* Raman analysis. Besides the emerged Raman signal assigned to dioxygen radical coupling and the peak at 936 cm^{-1} originating from ClO_4^- in the electrolyte, the characteristic Raman peaks of the $RuCoO_x$ do not change or shift as the potential increases (Figure 3f), suggesting the high structural stability of the $RuCoO_x$ under positive bias. In sharp contrast, an extra Raman band at around 580 cm^{-1} that is raised from the acidic soluble CoO_2 species[50,62,64] is observed at ≥1.36 V *vs* RHE for the Co_3O_4 (Figure 5e). This result is

almost consistent with the CV measurement (Figure 5d) and well explains the different acidic OER stability of the Co_3O_4 and $RuCoO_x$ (Figure 4d). It is noted that the weakening or even disappear of the CoO_2 characteristic peak at ≥ 1.56 V vs RHE is mainly ascribed to the high solubility of CoO_2 in acid. In addition, when the OER occurs at higher potentials, bubbles will be accumulated on the electrode surface, which would also reduce the Raman signal. It is also worth noting that the Raman signal corresponding to dioxygen radical coupling also emerges at high potentials (*e.g.*, 1.76 and 1.86 V vs RHE) for the Co_3O_4. This is not surprising since the ^{18}O isotope-labeled DEMS experiment has previously demonstrated that Co_3O_4 spinel can realize the diatomic O−O radical coupling in acid.[31]

The dissolution of Co species can further be indirectly reflected by the change in the Co^{III}/Co^{II} ratio (corresponding to integral area of A_{1g}/F_{2g} peaks) based on the *in situ* Raman analysis. The Co^{III}/Co^{II} ratio of the $RuCoO_x$ only slightly elevates upon the OER potentials (Figure 5f), suggesting the highly structural integrity of the $RuCoO_x$ under positive bias, well in line with the Co 2p XPS and CV analysis (Figure 5b,d). However, the ratio of Co^{III}/Co^{II} of the Co_3O_4 varies dramatically that it sharply rises to maximum at 1.46 V vs RHE and afterward significantly drops under higher potentials. The former can be attributed to the oxidation behavior of $Co^{II}Co^{III}/Co^{III}Co^{III}$, while the latter can be ascribed to the overoxidation of $Co^{III}Co^{III}$ to the acidic soluble $Co^{IV}Co^{IV}$ (*i.e.*, CoO_2) that results in a sharp decrease in Co_{oct} content. The difference in the Co^{III}/Co^{II} ratio of the Co_3O_4 and $RuCoO_x$ during the dynamic OER process also confirms the highly structural integrity of the Ru_{oct}−O−Co_{oct} collaborative coordination in the $RuCoO_x$ and thus the high acidic OER stability.

CONCLUSIONS

In summary, we have developed a highly active and robust $RuCoO_x$ catalyst through partial substitution of Co_{oct} sites in spinel Co_3O_4 by Ru atoms for enhanced acidic OER performance. Both the experimental and theoretical results confirmed that the resulted Ru_{oct}−O−Co_{oct} collaborative coordination with strong electron coupling effect can proceed the thermodynamically breakthrough heterogeneous DOM pathway. Meanwhile, the Ru_{oct}−O−Co_{oct} collaborative coordination can also gain electrons from surrounding electron-enriched Co_{tet} sites *via* bridging oxygen atoms, so that the overoxidation of active Ru_{oct} and Co_{oct} centers into acidic soluble RuO_4 and CoO_2 species can be suppressed. As a result, the $RuCoO_x$ catalyst with an ultralow Ru loading of 42.8 μg cm^{-2} delivers decent OER performance with only a 200 mV overpotential and a low degradation rate of 0.45 mV h^{-1} at 10 mA cm^{-2}. Our work not only establishes the $RuCoO_x$ as an efficient electrocatalysts for acidic OER, but also suggests an effective strategy to dramatically boost the acidic OER performance of Co_3O_4 and potentially the big family of spinel oxides by site preferential atomic substitution.

ASSOCIATED CONTENT

ⓢ Supporting Information

The Supporting Information is available free of charge at https://pubs.acs.org/doi/10.1021/jacs.3c05556.

Experimental section, theoretical calculation, and additional figures and tables (PDF)

AUTHOR INFORMATION

Corresponding Authors

Fen Yao − Key Laboratory of Preparation and Applications of Environmentally Friendly Material of the Ministry of Education, College of Chemistry, Jilin Normal University, Changchun 130103, China; Email: yaof@jlnu.edu.cn

Chung-Li Dong − Department of Physics, Tamkang University, New Taipei City 25137, Taiwan; orcid.org/0000-0002-4289-4677; Email: 148558@mail.tku.edu.tw

Qiu Jiang − School of Materials and Energy, University of Electronic Science and Technology of China, Chengdu 611731, China; Email: jiangqiu@uestc.edu.cn

Hanfeng Liang − State Key Laboratory of Physical Chemistry of Solid Surfaces, Tan Kah Kee Innovation Laboratory, College of Chemistry and Chemical Engineering, Xiamen University, Xiamen 361005, China; orcid.org/0000-0002-1778-3975; Email: hfliang@xmu.edu.cn

Authors

Weijie Zhu − State Key Laboratory of Physical Chemistry of Solid Surfaces, Tan Kah Kee Innovation Laboratory, College of Chemistry and Chemical Engineering, Xiamen University, Xiamen 361005, China

Kangjuan Cheng − School of Materials and Energy, University of Electronic Science and Technology of China, Chengdu 611731, China

Mengting Zhao − State Key Laboratory of Physical Chemistry of Solid Surfaces, Tan Kah Kee Innovation Laboratory, College of Chemistry and Chemical Engineering, Xiamen University, Xiamen 361005, China

Cheng-Jie Yang − Department of Physics, Tamkang University, New Taipei City 25137, Taiwan

Qiming Hong − State Key Laboratory of Physical Chemistry of Solid Surfaces, Tan Kah Kee Innovation Laboratory, College of Chemistry and Chemical Engineering, Xiamen University, Xiamen 361005, China

Zhoucheng Wang − State Key Laboratory of Physical Chemistry of Solid Surfaces, Tan Kah Kee Innovation Laboratory, College of Chemistry and Chemical Engineering, Xiamen University, Xiamen 361005, China

Complete contact information is available at:
https://pubs.acs.org/10.1021/jacs.3c05556

Author Contributions

The manuscript was written through contributions of all authors. All authors have given approval to the final version of the manuscript.

Notes

The authors declare no competing financial interest.

■ ABBREVIATIONS

OER	oxygen evolution reaction
PEMWE	proton exchange membrane water electrolyzer
LOM	lattice oxygen mechanism
AEM	adsorbate evolution mechanism
DOM	diatomic oxygen mechanism
Co_{oct}	octahedral Co
Co_{tet}	tetrahedral Co
SEM	scanning electron microscopy
SAED	selected area electron diffraction
HAADF-STEM	high-angle annular dark-field scanning transmission electron microscopy
XRD	X-ray diffraction
DFT	density functional theory
XAS	X-ray absorption spectrometry
EPR	electron paramagnetic resonance
CV	cyclic voltammetry
LSV	linear sweep voltammetry

■ REFERENCES

(1) Chen, Z.; Guo, L.; Pan, L.; Yan, T.; He, Z.; Li, Y.; Shi, C.; Huang, Z. F.; Zhang, X.; Zou, J. J. Advances in oxygen evolution electrocatalysts for proton exchange membrane water electrolyzers. *Adv. Energy Mater.* **2022**, *12*, 2103670.

(2) An, L.; Wei, C.; Lu, M.; Liu, H.; Chen, Y.; Scherer, G. G.; Fisher, A. C.; Xi, P.; Xu, Z. J.; Yan, C. H. Recent development of oxygen evolution electrocatalysts in acidic environment. *Adv. Mater.* **2021**, *33*, 2006328.

(3) Zhu, W.; Huang, Z.; Zhao, M.; Huang, R.; Wang, Z.; Liang, H. Hydrogen production by electrocatalysis using the reaction of acidic oxygen evolution: A review. *Environ. Chem. Lett.* **2022**, *20*, 3429−3452.

(4) Reier, T.; Oezaslan, M.; Strasser, P. Electrocatalytic oxygen evolution reaction (OER) on Ru, Ir, and Pt catalysts: A comparative study of nanoparticles and bulk materials. *ACS Catal.* **2012**, *2*, 1765−1772.

(5) Cherevko, S.; Geiger, S.; Kasian, O.; Kulyk, N.; Grote, J.-P.; Savan, A.; Shrestha, B. R.; Merzlikin, S.; Breitbach, B.; Ludwig, A.; Mayrhofer, K. J. J. Oxygen and hydrogen evolution reactions on Ru, RuO_2, Ir, and IrO_2 thin film electrodes in acidic and alkaline electrolytes: A comparative study on activity and stability. *Catal. Today* **2016**, *262*, 170−180.

(6) Zagalskaya, A.; Alexandrov, V. Mechanistic study of IrO_2 dissolution during the electrocatalytic oxygen evolution reaction. *J. Phys. Chem. Lett.* **2020**, *11*, 2695−2700.

(7) Wen, Y.; Chen, P.; Wang, L.; Li, S.; Wang, Z.; Abed, J.; Mao, X.; Min, Y.; Dinh, C. T.; Luna, P.; Huang, R.; Zhang, L.; Wang, L.; Wang, L.; Nielsen, R. J.; Li, H.; Zhuang, T.; Ke, C.; Voznyy, O.; Hu, Y.; Li, Y.; Goddard, W. A., III; Zhang, B.; Peng, H.; Sargent, E. H. Stabilizing highly active Ru sites by suppressing lattice oxygen participation in acidic water oxidation. *J. Am. Chem. Soc.* **2021**, *143*, 6482−6490.

(8) Shi, Z.; Li, J.; Wang, Y.; Liu, S.; Zhu, J.; Yang, J.; Wang, X.; Ni, J.; Jiang, Z.; Zhang, L.; Wang, Y.; Liu, C.; Xing, W.; Ge, J. Customized reaction route for ruthenium oxide towards stabilized water oxidation in high-performance PEM electrolyzers. *Nat. Commun.* **2023**, *14*, 843.

(9) Wohlfahrt-Mehrens, M.; Heitbaum, J. Oxygen evolution on Ru and RuO_2 electrodes studied using isotope labelling and on-line mass spectrometry. *J. Electroanal. Chem. Interfacial Electrochem.* **1987**, *237*, 251−260.

(10) Macounova, K.; Makarova, M.; Krtil, P. Oxygen evolution on nanocrystalline RuO_2 and $Ru_{0.9}Ni_{0.1}O_{2-\delta}$ electrodes - DEMS approach to reaction mechanism determination. *Electrochem. Commun.* **2009**, *11*, 1865−1868.

(11) Wang, J.; Yang, H.; Li, F.; LI, L. G.; Wu, J. B.; Liu, S. H.; Cheng, T.; Xu, Y.; Shao, Q.; Huang, X. Q. Single-site Pt-doped RuO_2 hollow nanospheres with interstitial C for high-performance acidic overall water splitting. *Sci. Adv.* **2022**, *8*, No. eabl927.

(12) Chen, S.; Huang, H.; Jiang, P.; Yang, K.; Diao, J.; Gong, S.; Liu, S.; Huang, M.; Wang, H.; Chen, Q. Mn-doped RuO_2 nanocrystals as highly active electrocatalysts for enhanced oxygen evolution in acidic media. *ACS Catal.* **2019**, *10*, 1152−1160.

(13) Su, J.; Ge, R.; Jiang, K.; Dong, Y.; Hao, F.; Tian, Z.; Chen, G.; Chen, L. Assembling ultrasmall copper-doped ruthenium oxide nanocrystals into hollow porous polyhedra: Highly robust electrocatalysts for oxygen evolution in acidic media. *Adv. Mater.* **2018**, 1801351.

(14) Chen, D.; Liu, T.; Wang, P.; Zhao, J.; Zhang, C.; Cheng, R.; Li, W.; Ji, P.; Pu, Z.; Mu, S. Ionothermal route to phase-pure RuB_2 catalysts for efficient oxygen evolution and water splitting in acidic media. *ACS Energy Lett.* **2020**, *5*, 2909−2915.

(15) Zhu, J.; Guo, Y.; Liu, F.; Xu, H.; Gong, L.; Shi, W.; Chen, D.; Wang, P.; Yang, Y.; Zhang, C.; Wu, J.; Luo, J.; Mu, S. Regulative electronic states around ruthenium/ruthenium disulphide heterointerfaces for efficient water splitting in acidic media. *Angew. Chem., Int. Ed.* **2021**, *60*, 12328−12334.

(16) Li, P.; Duan, X.; Kuang, Y.; Sun, X. Iridium in tungsten trioxide matrix as an efficient bi-functional electrocatalyst for overall water splitting in acidic media. *Small* **2021**, *17*, 2102078.

(17) Liu, X.; Xi, S.; Kim, H.; Kumar, A.; Lee, J.; Wang, J.; Tran, N. Q.; Yang, T.; Shao, X.; Liang, M.; Kim, M. G.; Lee, H. Restructuring highly electron-deficient metal-metal oxides for boosting stability in acidic oxygen evolution reaction. *Nat. Commun.* **2021**, *12*, 5676.

(18) Shi, Z. P.; Wang, Y.; Li, J.; Wang, X.; Wang, Y. B.; Li, Y.; Xu, W. L.; Jiang, Z.; Liu, C. P.; Xing, W.; Ge, J. J. Confined Ir single sites with triggered lattice oxygen redox: Toward boosted and sustained water oxidation catalysis. *Joule* **2021**, *5*, 2164−2176.

(19) Sun, S. C.; Jiang, H.; Chen, Z. Y.; Chen, Q.; Ma, M. Y.; Zhen, L.; Song, B.; Xu, C. Y. Bifunctional WC-supported RuO_2 nanoparticles for robust water splitting in acidic media. *Angew. Chem., Int. Ed.* **2022**, No. e202202519.

(20) Shi, Z.; Li, J.; Jiang, J.; Wang, Y.; Wang, X.; Li, Y.; Yang, L.; Chu, Y.; Bai, J.; Yang, J.; Ni, J.; Wang, Y.; Zhang, L.; Jiang, Z.; Liu, C.; Ge, J.; Xing, W. Enhanced acidic water oxidation by dynamic migration of oxygen species at the Ir/Nb_2O_{5-x} catalyst/support interfaces. *Angew. Chem., Int. Ed.* **2022**, *61*, No. e202212341.

(21) Mondschein, J. S.; Callejas, J. F.; Read, C. G.; Chen, J. Y. C.; Holder, C. F.; Badding, C. K.; Schaak, R. E. Crystalline cobalt oxide films for sustained electrocatalytic oxygen evolution under strongly acidic conditions. *Chem. Mater.* **2017**, *29*, 950−957.

(22) Li, A.; Kong, S.; Guo, C.; Ooka, H.; Adachi, K.; Hashizume, D.; Jiang, Q.; Han, H.; Xiao, J.; Nakamura, R. Enhancing the stability of cobalt spinel oxide towards sustainable oxygen evolution in acid. *Nat. Catal.* **2022**, *5*, 109−118.

(23) Huang, J.; Sheng, H.; Ross, R. D.; Han, J.; Wang, X.; Song, B.; Jin, S. Modifying redox properties and local bonding of Co_3O_4 by CeO_2 enhances oxygen evolution catalysis in acid. *Nat. Commun.* **2021**, *12*, 3036.

(24) Yang, X. L.; Li, H. N.; Lu, A. Y.; Min, S. X.; Idriss, Z.; Hedhili, M. N.; Huang, K. W.; Idriss, H.; Li, L. J. Highly acid-durable carbon coated Co_3O_4 nanoarrays as efficient oxygen evolution electrocatalysts. *Nano Energy* **2016**, *25*, 42−50.

(25) Zhou, Y.; Sun, S.; Wei, C.; Sun, Y.; Xi, P.; Feng, Z.; Xu, Z. J. Significance of engineering the octahedral units to promote the oxygen evolution reaction of spinel oxides. *Adv. Mater.* **2019**, *31*, 1902509.

(26) Kim, T. W.; Woo, M. A.; Regis, M.; Choi, K. S. Electrochemical synthesis of spinel type $ZnCo_2O_4$ electrodes for use as oxygen evolution reaction catalysts. *J. Phys. Chem. Lett.* **2014**, *5*, 2370−2374.

(27) Sun, S.; Sun, Y.; Zhou, Y.; Xi, S.; Ren, X.; Huang, B.; Liao, H.; Wang, L. P.; Du, Y.; Xu, Z. J. Shifting oxygen charge towards octahedral metal: A way to promote water oxidation on cobalt spinel oxides. *Angew. Chem., Int. Ed.* **2019**, *58*, 6042−6047.

(28) Lang, C.; Li, J.; Yang, K. R.; Wang, Y.; He, D.; Thorne, J. E.; Croslow, S.; Dong, Q.; Zhao, Y.; Prostko, G.; Brudvig, G. W.; Batista,

V. S.; Waegele, M. M.; Wang, D. Observation of a potential-dependent switch of water-oxidation mechanism on Co-oxide-based catalysts. *Chem* **2021**, *7*, 2101−2117.

(29) Plaisance, C. P.; van Santen, R. A. Structure sensitivity of the oxygen evolution reaction catalyzed by cobalt(II,III) oxide. *J. Am. Chem. Soc.* **2015**, *137*, 14660−14672.

(30) Dou, Y.; Liao, T.; Ma, Z.; Tian, D.; Liu, Q.; Xiao, F.; Sun, Z.; Ho Kim, J.; Xue Dou, S. Graphene-like holey Co₃O₄ nanosheets as a highly efficient catalyst for oxygen evolution reaction. *Nano Energy* **2016**, *30*, 267−275.

(31) Wang, N.; Ou, P.; Miao, R. K.; Chang, Y.; Wang, Z.; Hung, S. F.; Abed, J.; Ozden, A.; Chen, H. Y.; Wu, H. L.; Huang, J. E.; Zhou, D.; Ni, W.; Fan, L.; Yan, Y.; Peng, T.; Sinton, D.; Liu, Y.; Liang, H.; Sargent, E. H. Doping shortens the metal/metal distance and promotes OH coverage in non-noble acidic oxygen evolution reaction catalysts. *J. Am. Chem. Soc.* **2023**, *145*, 7829−7836.

(32) Wang, L.-P.; Van Voorhis, T. Direct-coupling O₂ bond forming a pathway in cobalt oxide water oxidation catalysts. *J. Phys. Chem. Lett.* **2011**, *2*, 2200−2204.

(33) Mavros, M. G.; Tsuchimochi, T.; Kowalczyk, T.; McIsaac, A.; Wang, L. P.; Voorhis, T. V. What can density functional theory tell us about artificial catalytic water splitting? *Inorg. Chem.* **2014**, *53*, 6386−6397.

(34) Lin, C.; Li, J.-L.; Li, X.; Yang, S.; Luo, W.; Zhang, Y.; Kim, S.-H.; Kim, D.-H.; Shinde, S. S.; Li, Y.-F.; Liu, Z.-P.; Jiang, Z.; Lee, J.-H. In-situ reconstructed Ru atom array on α-MnO₂ with enhanced performance for acidic water oxidation. *Nat. Catal.* **2021**, *4*, 1012−1023.

(35) Tripathy, S. K.; Christy, M.; Park, N. H.; Suh, E. K.; Anand, S.; Yu, Y. T. Hydrothermal synthesis of single-crystalline nanocubes of Co₃O₄. *Mater. Lett.* **2008**, *62*, 1006−1009.

(36) Shan, J.; Ye, C.; Chen, S.; Sun, T.; Jiao, Y.; Liu, L.; Zhu, C.; Song, L.; Han, Y.; Jaroniec, M.; Zhu, Y.; Zheng, Y.; Qiao, S. Z. Short-range ordered iridium single atoms integrated into cobalt oxide spinel structure for highly efficient electrocatalytic water oxidation. *J. Am. Chem. Soc.* **2021**, *143*, 5201−5211.

(37) Chuang, T. J.; Brundle, C. R.; Rice, D. W. Interpretation of the X-ray photoemission spectra of cobalt oxides and cobalt oxide surfaces. *Surf. Sci.* **1976**, *59*, 413−429.

(38) Oku, M.; Hirokawa, K. X-ray photoelectron spectroscopy of Co₃O₄, Fe₃O₄, Mn₃O₄, and related compounds. *J. Electron Spectrosc. Relat. Phenom.* **1976**, *8*, 475−481.

(39) Morgan, D. J. Resolving ruthenium: XPS studies of common ruthenium materials. *Surf. Interface Anal.* **2015**, *47*, 1072−1079.

(40) Shen, J. Y.; Adnot, A.; Kaliaguine, S. An ESCA study of the interaction of oxygen with the surface of ruthenium. *Appl. Surf. Sci.* **1991**, *51*, 47−60.

(41) Hou, L.; Li, Z.; Jang, H.; Wang, Y.; Cui, X.; Gu, X.; Kim, M. G.; Feng, L.; Liu, S.; Liu, X. Electronic and lattice engineering of ruthenium oxide towards highly active and stable water splitting. *Adv. Energy Mater.* **2023**, 2300177.

(42) Hao, S.; Liu, M.; Pan, J.; Liu, X.; Tan, X.; Xu, N.; He, Y.; Lei, L.; Zhang, X. Dopants fixation of ruthenium for boosting acidic oxygen evolution stability and activity. *Nat. Commun.* **2020**, *11*, 5368.

(43) Zhu, Y.; Wang, J.; Koketsu, T.; Kroschel, M.; Chen, J. M.; Hsu, S. Y.; Henkelman, G.; Hu, Z.; Strasser, P.; Ma, J. Iridium single atoms incorporated in Co₃O₄ efficiently catalyze the oxygen evolution in acidic conditions. *Nat. Commun.* **2022**, *13*, 7754.

(44) Tian, Y.; Wang, S.; Velasco, E.; Yang, Y.; Cao, L.; Zhang, L.; Li, X.; Lin, Y.; Zhang, Q.; Chen, L. A Co-doped nanorod-like RuO₂ electrocatalyst with abundant oxygen vacancies for acidic water oxidation. *iScience* **2020**, *23*, No. 100756.

(45) Wang, C.; Qi, L. Heterostructured inter-doped ruthenium-cobalt oxide hollow nanosheet arrays for highly efficient overall water splitting. *Angew. Chem., Int. Ed.* **2020**, *59*, 17219−17224.

(46) Okamura, M.; Kondo, M.; Kuga, R.; Kurashige, Y.; Yanai, T.; Hayami, S.; Praneeth, V. K.; Yoshida, M.; Yoneda, K.; Kawata, S.; Masaoka, S. A pentanuclear iron catalyst designed for water oxidation. *Nature* **2016**, *530*, 465−468.

(47) Kodera, M.; Kawahara, Y.; Hitomi, Y.; Nomura, T.; Ogura, T.; Kobayashi, Y. Reversible O-O bond scission of peroxodiiron(III) to high-spin oxodiiron(IV) in dioxygen activation of a diiron center with a bis-tpa dinucleating ligand as a soluble methane monooxygenase model. *J. Am. Chem. Soc.* **2012**, *134*, 13236−13239.

(48) Wang, B.; Zhao, K.; Yu, Z.; Sun, C.; Wang, Z.; Feng, N.; Mai, L.; Wang, Y.; Xia, Y. In situ structural evolution of the multi-site alloy electrocatalyst to manipulate the intermediate for enhanced water oxidation reaction. *Energy Environ. Sci.* **2020**, *13*, 2200−2208.

(49) Zhang, M.; de Respinis, M.; Frei, H. Time-resolved observations of water oxidation intermediates on a cobalt oxide nanoparticle catalyst. *Nat. Chem.* **2014**, *6*, 362−367.

(50) Moysiadou, A.; Lee, S.; Hsu, C. S.; Chen, H. M.; Hu, X. Mechanism of oxygen evolution catalyzed by cobalt oxyhydroxide: Cobalt superoxide species as a key intermediate and dioxygen release as a rate-determining step. *J. Am. Chem. Soc.* **2020**, *142*, 11901−11914.

(51) Takashi, S.; Masayasu, M. Raman and infrared spectra of μ-O₂ dicobalt(III) complexes. *Bull. Chem. Soc. Jpn.* **1978**, *51*, 1374−1379.

(52) Lee, S.; Banjac, K.; Lingenfelder, M.; Hu, X. Oxygen isotope labeling experiments reveal different reaction sites for the oxygen evolution reaction on nickel and nickel iron oxides. *Angew. Chem., Int. Ed.* **2019**, *58*, 10295−10299.

(53) Wang, X.; Wan, X.; Qin, X.; Chen, C.; Qian, X.; Guo, Y.; Xu, Q.; Cai, W.-B.; Yang, H.; Jiang, K. Electronic structure modulation of RuO₂ by TiO₂ enriched with oxygen vacancies to boost acidic O₂ evolution. *ACS Catal.* **2022**, *12*, 9437−9445.

(54) Wei, C.; Rao, R. R.; Peng, J.; Huang, B.; Stephens, I. E. L.; Risch, M.; Xu, Z. J.; Shao-Horn, Y. Recommended practices and benchmark activity for hydrogen and oxygen electrocatalysis in water splitting and fuel cells. *Adv. Mater.* **2019**, *31*, 1806296.

(55) Liang, H.; Cao, Z.; Xia, C.; Ming, F.; Zhang, W.; Emwas, A.-H.; Cavallo, L.; Alshareef, H. N. Tungsten blue oxide as a reusable electrocatalyst for acidic water oxidation by plasma-induced vacancy engineering. *CCS Chem.* **2021**, *3*, 1553−1561.

(56) Li, A.; Ooka, H.; Bonnet, N.; Hayashi, T.; Sun, Y.; Jiang, Q.; Li, C.; Han, H.; Nakamura, R. Stable potential windows for long-term electrocatalysis by manganese oxides under acidic conditions. *Angew. Chem., Int. Ed.* **2019**, *58*, 5054−5058.

(57) Geiger, S.; Kasian, O.; Ledendecker, M.; Pizzutilo, E.; Mingers, A. M.; Fu, W. T.; Diaz-Morales, O.; Li, Z.; Oellers, T.; Fruchter, L.; Ludwig, A.; Mayrhofer, K. J. J.; Koper, M. T. M.; Cherevko, S. The stability number as a metric for electrocatalyst stability benchmarking. *Nat. Catal.* **2018**, *1*, 508−515.

(58) Wu, Z.-Y.; Chen, F.-Y.; Li, B.; Yu, S.-W.; Finfrock, Y. Z.; Meira, D. M.; Yan, Q.-Q.; Zhu, P.; Chen, M.-X.; Song, T.-W.; Yin, Z.; Liang, H.-W.; Zhang, S.; Wang, G.; Wang, H. Non-iridium-based electro-catalyst for durable acidic oxygen evolution reaction in proton exchange membrane water electrolysis. *Nat. Mater.* **2022**, *22*, 100−108.

(59) He, J.; Chen, W.; Gao, H.; Chen, Y.; Zhou, L.; Zou, Y.; Chen, R.; Tao, L.; Lu, X.; Wang, S. Tuning hydrogen binding modes within RuO₂ lattice by proton and electron co-doping for active and stable acidic oxygen evolution. *Chem. Catal.* **2022**, *2*, 578−594.

(60) Wang, K.; Wang, Y.; Yang, B.; Li, Z.; Qin, X.; Zhang, Q.; Lei, L.; Qiu, M.; Wu, G.; Hou, Y. Highly active ruthenium site stabilized by modulating electron-feeding for sustainable acidic oxygen-evolution electrocatalysis. *Energy Environ. Sci.* **2022**, *15*, 2356−2365.

(61) Risch, M.; Ringleb, F.; Kohlhoff, M.; Bogdanoff, P.; Chernev, P.; Zaharieva, I.; Dau, H. Water oxidation by amorphous cobalt-based oxides: In situ tracking of redox transitions and mode of catalysis. *Energy Environ. Sci.* **2015**, *8*, 661−674.

(62) Yao, N.; Wang, G.; Jia, H.; Yin, J.; Cong, H.; Chen, S.; Luo, W. Intermolecular energy gap-induced formation of high-valent cobalt species in CoOOH surface layer on cobalt sulfides for efficient water oxidation. *Angew. Chem., Int. Ed.* **2022**, *61*, No. e202117178.

(63) Zhou, J.; Wang, Y.; Su, X. Z.; Gu, S. Q.; Liu, R. D.; Huang, Y. B.; Yan, S.; Li, J.; Zhang, S. Electrochemically accessing ultrathin Co (oxy)-hydroxide nanosheets and operando identifying their active

phase for the oxygen evolution reaction. *Energy Environ. Sci.* **2019**, *12*, 739−746.

(64) Chen, Z.; Cai, L.; Yang, X.; Kronawitter, C.; Guo, L.; Shen, S.; Koel, B. E. Reversible structural evolution of $NiCoO_xH_y$ during the oxygen evolution reaction and identification of the catalytically active phase. *ACS Catal.* **2018**, *8*, 1238−1247.

(65) Bratsch, S. G. Standard electrode potentials and temperature coefficients in water at 298.15 k. *J. Phys. Chem. Ref. Data* **1989**, *18*, 1−21.